

Elastic and inelastic scattering of π^+ and π^- on ^{12}C at 995 MeV/cK. Aoki,¹ H. Sakaguchi,² N. Nose-Togawa,³ T. Takahashi,¹ T. Hasegawa,⁴ O. Hashimoto,⁵ T. Nagae,¹ M. Sekimoto,¹ A. Ohkusu,⁶ H. Bhang,⁷ H. Yu,⁷ and Y. Gavrilo⁸¹*High Energy Accelerator Research Organization (KEK), Tsukuba, Ibaraki 305-0801, Japan*²*Department of Applied Physics, Miyazaki University, Miyazaki 889-2192, Japan*³*Research Center for Nuclear Physics (RCNP), Ibaraki, Osaka 567-0047, Japan*⁴*School of Allied Health Sciences, Kitazato University, Sagami-hara 228-8555, Japan*⁵*Department of Physics, Tohoku University, Sendai 980-8578, Japan*⁶*Department of Physics, Osaka University, Toyonaka, Osaka 560-0043, Japan*⁷*Department of Physics, Seoul National University, Seoul 151-742, Korea*⁸*Institute for Nuclear Research, Academy of Science of Russia, Moscow, Russia*

(Received 20 March 2007; published 24 August 2007)

π^+ and π^- elastic and inelastic scattering to the 2_1^+ (4.44 MeV) state on ^{12}C at 995 MeV/c were measured over an angular range for elastic-scattering from 5.4° to 28.2° and for inelastic scattering from 15.2° to 22.8° . Both of the elastic-scattering data sets were well reproduced by first-order factorized momentum-space optical potential calculations with free π - N elementary amplitudes and three different ground state densities, which were deduced from the charge density and microscopic model calculations, the cluster model and the shell model. We also extracted σ_{tot} , σ_{el} , and σ_R phenomenologically and compared them with a Fermi averaging model. The inelastic cross sections of π^+ - ^{12}C and π^- - ^{12}C were compared with the DWIA calculations, one using the transition density ($0^+ \rightarrow 2_1^+$) deduced by the cluster model and the other using the transition density deduced by the shell model.

DOI: [10.1103/PhysRevC.76.024610](https://doi.org/10.1103/PhysRevC.76.024610)

PACS number(s): 25.80.Dj, 25.80.Ek, 27.20.+n, 13.75.-n

I. INTRODUCTION

In pion-nucleus scattering above the Δ -resonance energy, the elementary amplitude becomes forward peaked and the pions interact moderately. Accordingly, an agreement between theoretical calculations and the experimental data is expected. However, experimental studies of the pion-nucleus interaction using pions in the GeV/c region as a probe to investigate nuclear structures are scarce [1–3] compared with studies at lower energies. Especially experimental studies of the inelastic scattering in the GeV/c region are rare [1].

In our previous article, we reported on our systematic measurements of differential cross sections of π^- elastic scattering from ^{12}C above the Δ -resonance region [3]. Comparing our data with the first-order optical potential model calculation (PIPIT) [4], we found that the PIPIT calculation reproduces the magnitude of the cross section in the forward region better, as we increase incident pion momenta from 610 to 895 MeV/c. Also, we found that our data at 790 MeV/c were consistent within the systematic errors with the data at 800 MeV/c, which were measured at Brookhaven National Laboratory (BNL) and were reported to show the deviation from the first-order optical potential model calculation (KPIT) [1]. The magnitude of our elastic data was located between the BNL data and the PIPIT calculation.

They also reported the inelastic-scattering data (4.4 MeV 2_1^+ and 9.6 MeV 3_1^- for both π^- - ^{12}C and π^+ - ^{12}C) and compared the differential cross sections with the DWBA calculation (NDWPI). In the case of inelastic scattering, the discrepancy between the data and the calculations is larger than that of the elastic scattering. It is important to confirm any

disagreement with theoretical calculations by measuring the experimental differential cross sections under well-controlled systematic errors using a spectrometer having good energy resolution.

In this report, we present our precise measurements of the cross sections for π^+ and π^- elastic and inelastic scattering to the 2_1^+ (4.44 MeV) state on ^{12}C at an incident momentum of 995 MeV/c using the SKS (superconducting kaon spectrometer) at KEK [5]. The SKS has properties, including good energy resolution and a large solid angle using meson beams in the GeV/c region, which make it possible for us to perform precise measurements of the angular distributions of differential cross sections with small systematic errors. As a result, normalization factors to deduce the cross section were not necessary for our experimental data. We selected an incident pion beam momentum of 995 MeV/c, because in this incident momentum region, there is the largest difference between the π^+ - p and π^- - p total cross sections except for the Δ -resonance region. Thus, we decided to measure the differential cross sections using both π^+ and π^- beams to confirm that there is no difference between the proton distribution and the neutron distribution inside the ^{12}C nucleus for future use of neutron skin searches with pion beams.

In Sec. II the experimental apparatus is described in detail. In Sec. III, the procedures of data deduction to minimize any systematic errors of the cross sections are described. The experimental data are given in Sec. IV along with an explanation of systematic errors. In Sec. V we compare the data with theoretical model calculations. A summary of the work is given in Sec. VI.

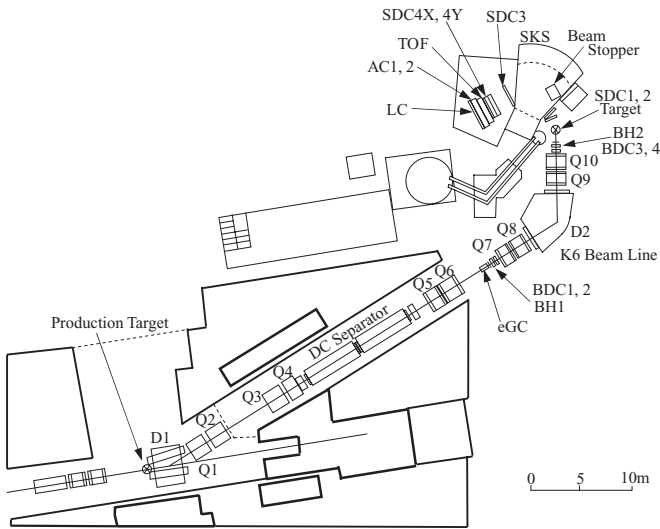


FIG. 1. Schematic view of the experimental setup.

II. EXPERIMENT

The experiment was performed at the K6 beam line of the North Counter Hall of the KEK 12-GeV PS (Proton Synchrotron) using the SKS. The beam momentum of both the negative and positive pions was set at 995 MeV/c. Figure 1 shows the experimental setup.

A. Beam spectrometer

The pion beam was identified and the beam momentum was analyzed with the beam spectrometer system at the K6 beam line.

Pions were produced in a production target (Pt, $6 \text{ mm}^\phi \times 60 \text{ mm}^L$), separated with the D1 magnet and selected with electrostatic separators in the K6 beamline at the first stage. After separators and Q magnets, pions entered into the beamline spectrometer system where they were well identified with an electron gas Čerenkov counter (eGC) and time-of-flight (TOF) between two timing hodoscope counters (BH1 and BH2). The eGC was used to reject electrons. The TOF between BH1 and BH2 was used to reject heavier particles, such as protons. BH1 and BH2 were also used as an on-line triggers with other timing counters behind the target. Target veto scintillators (TV) were also used to ensure that the beam particle passed through the target. Thus, the beam was defined by $\text{BH1} \otimes \text{BH2} \otimes \overline{\text{eGC}} \otimes \overline{\text{TV}}$.

In the normal setup, decayed muons from the beam pions were not distinguished because the mass and velocity were close to pion ones. We conducted other separated runs to measure muon contamination in the beam with a muon gas Čerenkov counter (μGC) placed at the target point. The μGC is a high-pressure freon gas Čerenkov counter that is compact enough to be placed at the target area.

The beam momentum was analyzed by the QQDQQ (Q7, Q8, D2, Q9, and Q10) system with high-rate drift chambers (BDC1-4). BDC1 and BDC2 were set upstream, and BDC3

and BDC4 were located downstream of the QQDQQ system. Each BDC was composed of six planes (x, x', u, u', v, v') with a 5-mm cell size. The BDCs were used to measure the beam trajectory both before and after the QQDQQ system with an accuracy of $\sigma \approx 250 \mu\text{m}$ in position resolution. The BDCs could be operated at a high counting rate up to a few MHz to count the beam particles. The momentum of a beam pion was reconstructed with a third-order transport matrix of the QQDQQ system for each event.

B. Scattered-particle spectrometer

After the experimental target, scattered pions were measured with the SKS, which was composed of a large superconducting dipole magnet (the SKS magnet), drift chambers (SDC1,2 before the SKS magnet and SDC3, 4X, 4Y, after the SKS magnet), and trigger counters (TOF wall and LC wall). Although two layers of aerogel Čerenkov counters (AC1, AC2) were located between the TOF wall and the LC wall, we did not use AC1 and AC2 in the present experiment. The SKS spectrometer has a large acceptance of 100 msr ($\pm 15^\circ$ horizontal and $\pm 5^\circ$ vertical) and good momentum resolution, $\Delta p/p \sim 0.1\%$ (FWHM). The trigger counters were composed of a scintillator wall to measure the TOF and a Lucite Čerenkov counter wall (LC) to reject protons. A scattered pion was triggered with $\text{TOF} \otimes \text{LC}$. The momentum of the scattered particle was resolved by the Runge-Kutta method using information about the hit positions by the tracking drift chambers and the previously measured precise magnetic field map.

SDC1 and SDC2 of the tracking drift chamber were set in front of the SKS magnet after the target. They had the same drift-cell structure as the BDC and could be operated at a high counting rate. SDC3, 4X, and 4Y of the tracking drift chamber, which had the wire spacing of 21 mm, were installed at the exit of the SKS magnet.

It is difficult to separate elastically scattered pions from the beam pions, because they have almost the same momentum. To measure scattered pions as far forward as possible (around 5°) and to measure them beyond the second peak (to around 27°), we used the following methods:

(i) A stack of lead blocks ($30 \text{ cm}^W \times 40 \text{ cm}^H \times 50 \text{ cm}^L$) was installed at the entrance gap of the SKS magnet as a beam stopper to prevent the beam events from hitting the downstream detectors, which could not accept a high rate counting.

(ii) We separately measured angular setup 1 (about 5° – 18°) and angular setup 2 (about 11° – 28°) because the cross section for the pion elastic scattering is very different between the forward angles and others. At 5° it is about 1000 times larger than that at 25° . In both angular setups, the SKS spectrometer system was placed at the same position where the central track was 14° . In angular setup 2, we used a veto scintillator (SAV) placed in front of a portion of SDC2 to reject forward-scattered particles from triggers. We took more time to measure the cross section in the angular setup 2 than setup 1, and we also used a two-times thicker carbon target in angular setup 2.

C. Beams and targets

The beam intensity was adjusted to keep the data-acquisition dead time at less than 10%. The typical beam intensity was 4×10^5 particles/spill for angular setup 1 and 1×10^6 particles/spill for angular setup 2. The typical trigger rate was 500-800 events/spill. The spill interval was 4 sec and its duration was 1.2 sec.

The K6 beam transport was tuned to focus between the target and the beam stopper, a stack of lead blocks in the gap of the SKS magnet, because we needed as many beam particles as possible, and the beam had to be stopped at the narrow beam stopper. The typical beam size at the target was about 2 cm (X-horizontal) \times 4 cm (Y-vertical) (FWHM). The angular divergency of the beam were about ± 30 mrad (dx/dz -horizontal) and ± 20 mrad (dy/dz -vertical).

The number of beam particles was counted with a counter simultaneously in the π - ^{12}C and π - p scattering experiments. However, to confirm the possible efficiency of the beam without any influence of the scattered particle triggers, separated beam trigger runs with BH1 \otimes BH2 \otimes eGC \otimes TV were necessary.

To measure the elastic and inelastic scattering from carbon, a natural-carbon target of 10 cm \times 10 cm \times 0.89 g/cm² was used in angular setup 1 and 10 cm \times 10 cm \times 1.78 g/cm² in angular setup 2. For the purpose of examining the absolute cross section, a plastic scintillator target of 7 cm^W \times 9 cm^H \times 1.97 g/cm² (BICRON BC-408) was used to measure the π - p elastic cross section and also the π - ^{12}C elastic and inelastic cross sections.

Moreover, we used veto scintillators (TV) on both sides of the target to reject those events that were triggered by beam particles without hitting the target.

III. DATA REDUCTION PROCEDURES

One of our purposes is to deduce the cross section precisely. To fulfill this, we need appropriate software cuts in the analysis, suitable fitting functions to extract target events, and careful estimations of the efficiencies.

Considering the efficiencies with software cuts, the differential cross section is reproduced as follows:

$$\frac{d\sigma}{d\Omega}(\theta) = Y(\theta) \frac{1}{N_{\text{tgt}} N_{\text{beam}}} \frac{1}{\Delta\Omega_{\text{eff}}(\theta)} \frac{1}{\varepsilon(\theta)}, \quad (1)$$

$$N_{\text{beam}} = N_{\text{scaler}} \varepsilon_{\text{K6prof}} \varepsilon_{\text{K6mom}} R_{\pi\mu}, \quad (2)$$

$$\Delta\Omega_{\text{eff}}(\theta) = \Delta\Omega(\theta) [1 - \varepsilon_{\text{de-es}}(\theta)] (1 - \varepsilon_{\text{abs}}), \quad (3)$$

$$\varepsilon(\theta) = \varepsilon_{\text{DAQ}} \varepsilon_{\text{K6}} \varepsilon_{\text{SKS}}(\theta) \varepsilon_{\text{vertex}}, \quad (4)$$

$$\varepsilon_{\text{K6}} = \varepsilon_{\text{BH1-BH2}} \varepsilon_{\text{BDC}} \varepsilon_{\text{K6track}}, \quad (5)$$

$$\varepsilon_{\text{SKS}}(\theta) = \varepsilon_{\text{TOF-LC}} \varepsilon_{\text{SDC12}}(\theta) \varepsilon_{\text{SDC34}} \times \varepsilon_{\text{SKStrack}}(\theta) \varepsilon_{\text{SKScut}}(\theta), \quad (6)$$

where $Y(\theta)$ is the yield at the scattering angle θ , N_{tgt} is the target areal density, N_{beam} is the incident pion flux, $\Delta\Omega_{\text{eff}}(\theta)$ is the effective solid angle and $\varepsilon(\theta)$ is the total efficiency, including various experimental and analysis efficiencies, the definitions of which are described in Table I. N_{scaler} is the scaler counts of BH1 \otimes BH2 \otimes eGC.

TABLE I. Definition and typical values of the efficiencies. The typical values show examples of the π^- - ^{12}C angular setup 2.

Efficiencies	Description	Typical value (%)	Relative error (%)
$\varepsilon_{\text{K6prof}}$	Efficiency of beam profile cut	93.4 ± 0.5	0.5
$\varepsilon_{\text{K6mom}}$	Efficiency of beam momentum cut	26.8 ± 0.2	0.7
$R_{\pi\mu}$	Pion ratio in beam	96.7 ± 2.2	2.3
$1 - \varepsilon_{\text{de-es}}(\theta)$	Survival rate in trigger condition after scattering considering pion-decay to muon	$96.9 \pm 1.4^{\text{a,b}}$	1.4
$1 - \varepsilon_{\text{abs}}$	Nonabsorption rate of scattered pion	90.6 ± 2.3	2.5
ε_{DAQ}	Data acquisition efficiency	90.1 ± 0.1	0.1
$\varepsilon_{\text{BH1-BH2}}$	Analysis efficiency of beam line trigger counters (BH1, BH2)	96.6 ± 0.4	0.4
ε_{BDC}	BDC efficiency	82.1 ± 0.4	0.5
$\varepsilon_{\text{K6track}}$	Analysis efficiency of beam-momentum reconstruction	94.8 ± 0.5	0.5
$\varepsilon_{\text{TOF-LC}}$	Efficiency of SKS trigger counters (TOF, LC)	91.4 ± 0.3	0.3
$\varepsilon_{\text{SDC12}}(\theta)$	SDC12 efficiency	$77.3 \pm 1.7^{\text{a}}$	2.2
$\varepsilon_{\text{SDC34}}$	SDC34 efficiency	94.9 ± 0.1	0.1
$\varepsilon_{\text{SKStrack}}(\theta)$	Analysis efficiency of SKS momentum reconstruction	$94.3 \pm 0.9^{\text{a}}$	1.0
$\varepsilon_{\text{SKScut}}(\theta)$	Software cut (χ^2 cut) efficiency in SKS tracking	$85.0 \pm 0.9^{\text{a}}$	1.1
$\varepsilon_{\text{vertex}}$	Efficiency of event vertex cut	100.0 ± 0.0	0.0

^aTypical value at $\theta_{\text{lab.}} = 14^\circ$.

^bCalculated in the effective solid angle ($\Delta\Omega'_{\text{eff}}(\theta)$) simulation.

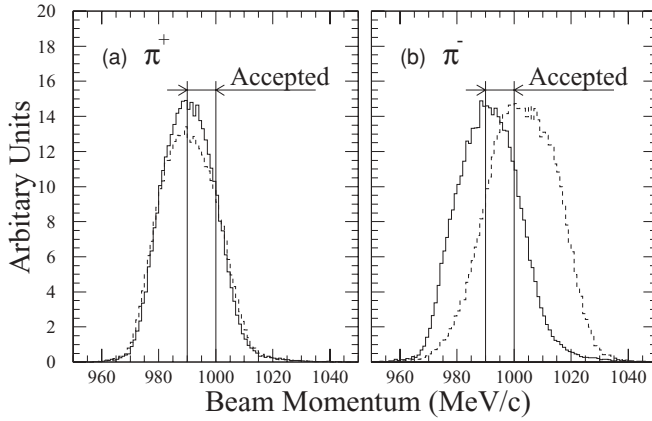


FIG. 2. Beam-momentum distributions at the target. The solid line shows angular setup 1 and the dashed line shows angular setup 2 in both figures. (a) π^+ beam momenta. (b) π^- beam momenta. The beam-momentum distribution of the angular setup 2 is shifted to higher values. A tight beam-momentum cut ($990 \text{ MeV}/c < P_{\text{beam}} < 1000 \text{ MeV}/c$) was needed to match the $p(\pi^-, \pi^-)p$ data in the overlapped region between angular setups 1 and 2.

A. Software cuts

In the analysis, we needed many software cuts as follows before extracting the number of the event:

- (i) A multiplicity of one was required in all hodoscope trigger counters (BH1, BH2, TOF, and LC).
- (ii) The TOF of the beam between BH1 and BH2 was required to be within the window for pions.
- (iii) Reconstructed beam tracks of the inlet and outlet of the QQDQQ in the beam spectrometer were required to be below a reasonable χ^2 .
- (iv) Deduced beam profiles at the target were required to be within a reasonable size and direction in both the horizontal and vertical directions.
- (v) Reconstructed beam momenta were selected within a narrow width, from 990 to 1000 MeV/c . We obtained a slightly different beam momentum distribution for π^- beam experiments of the angular setup 2, as shown by the dashed curve in Fig. 2(b). The peak of the beam-momentum distribution of the angular setup 2 shifted to 1002 MeV/c , whereas the peak of the angular setup 1 was 990 MeV/c . Without a beam momentum cut, we could not obtain good agreement of the $p(\pi^-, \pi^-)p$ cross section in the overlapped region between angular setups 1 and 2. After introducing a beam-momentum cut, we could obtain good agreement.
- (vi) The TOF of the scattered particles between the TOF and LC counters was required to be within reasonable windows.
- (vii) The track in the SKS was reconstructed with a reasonable χ^2 value.
- (viii) The event vertex (reconstructed from the beam track and the scattered particle track) was required to be within the target volume.

The scattering angle was calculated by the angle between the trajectories of the beam track and the scattered particle track. The angular resolution was confirmed to be 0.14° (rms) by different beam-through-runs. The excitation energy was kinematically calculated based on information about the scattering angle, the beam momentum and the scattered particle momentum. We also considered the energy loss in the target, where we assumed that all particles were scattered at the half thickness of the target. These software cuts were taken into account as parts of the efficiencies to derive the differential cross section.

B. Peak fitting

The yields were extracted by fitting the energy spectrum $[Y(\theta)]$ after considering the efficiencies. For $\pi^+{}^{12}\text{C}$ and $\pi^-{}^{12}\text{C}$ scattering, we used the spectrum with four peaks corresponding to the ground state as well as the 2_1^+ (4.44 MeV), 0_2^+ (7.65 MeV), and 3_1^- (9.64 MeV) states. Because the 0_2^+ excitation is weak and the 3_1^- peak is affected by the higher physical continuum, we adopted only the ground state and the 2_1^+ state events, extracted as our experimental data. Figure 3 shows the excitation spectra and the best-fitting functions (Function 3) for four scattering angles. In energy regions higher than the 3_1^- , the physical continuum can be seen. The peak shape was defined by the ground-state peak at forward angles where the ground state is dominant compared with the inelastic-scattering states, which are less than 1%. We examined three types of fitting functions for a peak:

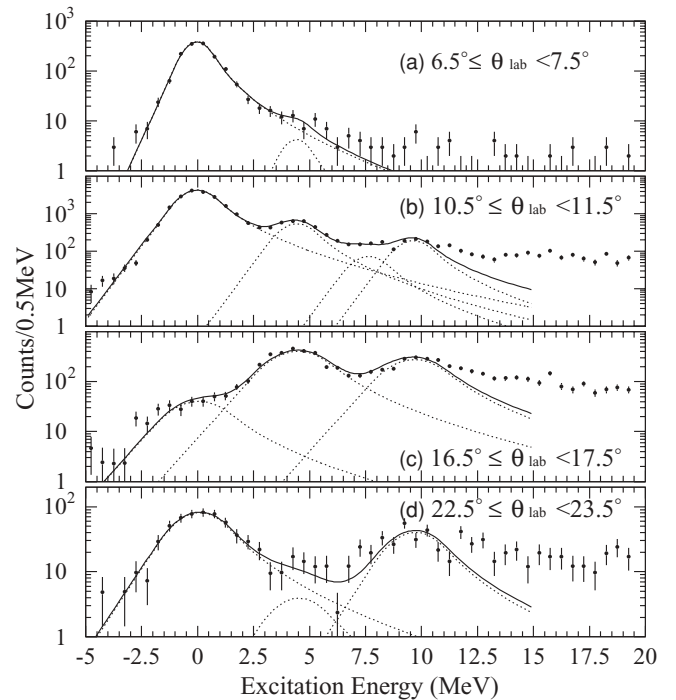


FIG. 3. Fitting the excitation energy spectra. Each histogram has the summed events within 1° in the laboratory frame. The solid curves show the results of the best fitting (Function 3). The dotted curves show each simple peak that composes the best fitting.

$$\begin{aligned}
\text{Function 1: } f_1(x) &= \begin{cases} a \exp \left\{ -\frac{(x-p)^2}{2\sigma^2} \right\} & (x \leq p + \sigma), \\ a \exp \left\{ -\frac{x-p}{\sigma} + \frac{1}{2} \right\} & (p + \sigma < x); \end{cases} \\
\text{Function 2: } f_2(x) &= \begin{cases} b \exp \left\{ -\frac{(x-p)^2}{2\sigma^2} \right\} & (x \leq p + \sigma), \\ b \exp \left\{ -\frac{x-p}{\sigma} + \frac{1}{2} \right\} & (p + \sigma < x \leq p + \frac{3}{2}\sigma), \\ b \sqrt{\frac{3\sigma}{2(x-p)}} \exp \left\{ -2\sqrt{\frac{2(x-p)}{3\sigma}} + 1 \right\} & (p + \frac{3}{2}\sigma < x); \end{cases} \\
\text{Function 3: } f_3(x) &= \begin{cases} c \exp \left\{ \frac{3}{2} \frac{(x-p)}{\sigma} + \frac{9}{8} \right\} & (x \leq p - \frac{3}{2}\sigma), \\ c \exp \left\{ -\frac{(x-p)^2}{2\sigma^2} \right\} & (p - \frac{3}{2}\sigma < x \leq p + \sigma), \\ c \exp \left\{ -\frac{x-p}{\sigma} + \frac{1}{2} \right\} & (p + \sigma < x \leq p + \frac{3}{2}\sigma), \\ c \sqrt{\frac{3\sigma}{2(x-p)}} \exp \left\{ -2\sqrt{\frac{2(x-p)}{3\sigma}} + 1 \right\} & (p + \frac{3}{2}\sigma < x). \end{cases}
\end{aligned}$$

These fitting functions have Gaussian shapes and asymmetric tails longer on the high-excitation energy side than on the low-excitation energy side. When we fitted with these functions to four peaks, we fixed the energy difference for the excitation states (4.44, 7.65, and 9.64 MeV above the ground state). We also used the same width parameter (σ) for the four peaks at the same angle.

When we compared the χ^2 of the fitting, Function 3 gave the smallest χ^2 . We adopted Function 3 to extract the areas. The differences in the areas among fitting functions are considered to be a systematic error.

For $\pi^+ - p$ and $\pi^- - p$ scattering, there was the background from ^{12}C because we used a scintillator target where ^{12}C was included. Before fitting with Function 3, we subtracted the background using the $\pi - ^{12}\text{C}$ scattering data from ^{12}C target, as shown in Fig. 4.

C. Efficiencies

It is very important to obtain efficiencies precisely to deduce the absolute differential cross section. Regarding efficiencies, there are two categories. One is the intrinsic efficiency for each detector. The other is the analysis efficiencies, which originated from the analysis algorithm, software cuts and so on. For the tracking drift chambers, the intrinsic inefficiency was negligible, because we prepared redundant planes. As for the typical timing counter, TOF and LC have intrinsic efficiencies of more than 99.8%.

The analysis efficiencies could be estimated as follows:

$$\varepsilon = \frac{\text{number of accepted events after analysis}}{\text{number of true events to be analyzed}}. \quad (7)$$

The denominator means those events regarded as being true, from which any fake triggered events were previously removed. Table I shows the definition and the typical value of the efficiencies. All beam efficiencies ($\varepsilon_{\text{K6prof}}$, $\varepsilon_{\text{K6mom}}$, $\varepsilon_{\text{BH1-BH2}}$, ε_{BDC} , and $\varepsilon_{\text{K6track}}$) were estimated using other beam trigger runs to exclude any trigger bias for the scattered particles.

It is very important to precisely estimate the pion-muon ratio in the beam, $R_{\pi\mu}$, to deduce the absolute differential cross section without any normalization factor. In our trigger system, most of the contamination in the beam came from muons decayed from beam pions; we could not separate these decayed muons. We measured the muon number at the target position with the muon gas Čerenkov counter (μ -GC) in each separate run and compared it with simulations using DECAY TURTLE [6]. Table II gives these results. Because the μ -GC counts particles above the threshold β , we need the simulation to consider decayed muons below the threshold. Our experimental results in the second column agree with the simulation results above the threshold in the third column within 2.5%. Taking account of this agreement, we adopted a total simulation result involving muons below the threshold as the muon contamination ratio in the beam. The difference between the experimental data and the simulation above the threshold was considered to be a systematic error.

For SDC12, there was no other detectors behind SDC2 to prove that the track passed through the effective area of the SDC1 and SDC2. Therefore, we used the hit information of SDC12 itself to define the analysis efficiency. The SDC12 analysis efficiency is defined as

$$\varepsilon_{\text{SDC12}} = \varepsilon_{\text{tag}} \varepsilon_{\text{est}}, \quad (8)$$

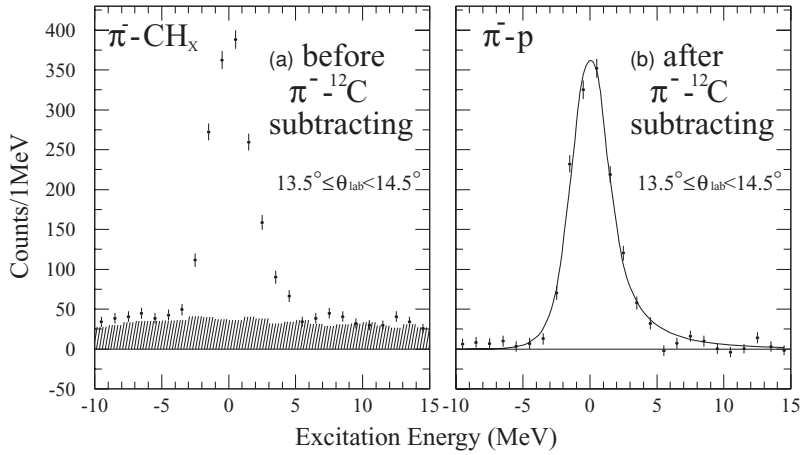


FIG. 4. Excitation energy spectra to extract $p(\pi^-, \pi^-)p$. (a) Raw spectrum taken with a scintillator target (CH_x), where the hatched area shows the contribution of $^{12}\text{C}(\pi^-, \pi^-)^{12}\text{C}$ taken with a carbon target. (b) $^{12}\text{C}(\pi^-, \pi^-)^{12}\text{C}$ background was subtracted from the raw spectrum. The histogram means the $p(\pi^-, \pi^-)p$ spectrum. The solid line shows the best-fitting result (Function 3).

where ε_{tag} is the efficiency to hit more than four planes of six planes of SDC1 and three planes of four planes of SDC2, which was calculated from the intrinsic efficiencies for each plane; ε_{est} means the ratio of accepted events after analysis. The typical value was 98% for ε_{tag} and 79% for ε_{est} from the example of $\pi^-^{12}\text{C}$ angular setup 2. The reason for the low ε_{est} is attributed to a χ^2 cut in the analysis procedure. The contribution from accidental hits was estimated to be less than 1% and thus is negligible.

For $\varepsilon_{\text{SDC34}}$, we could use the hit information of the TOF and LC to define a track that passed through the effective area of SDC3 and SDC4. The position dependence was negligible. $\varepsilon_{\text{SKStrack}}$ and $\varepsilon_{\text{SKScut}}$ were estimated according to Eq. (7) at each angle. A small dependence on the scattering angle was observed. $\varepsilon_{\text{de-es}}$ and $1 - \varepsilon_{\text{abs}}$ are explained in Sec. III D.

D. Effective solid angle of the spectrometer

For scattered-particle analysis, we could not separate muons generated in pion decay from scattered pions because the mass and momentum were similar to each other. Some decay muons escaped from the effective detector volume with large

decay angles, the ratio of which is represented as $\varepsilon_{\text{de-es}}$. We took into account this efficiency, $1 - \varepsilon_{\text{de-es}}$, calculating the effective solid angle. We calculated the effective solid angle with the pions and generated muons involved in the effective detector volume and excluded the muons that escaped out of the effective detector volume. We obtained $96.9 \pm 1.4\%$ as a typical value for $1 - \varepsilon_{\text{de-es}}$ from this calculation, using a Monte Carlo simulation code, GEANT [7]. Moreover, for scattered pions, we calculated the nonabsorption rate of scattered pions, $1 - \varepsilon_{\text{abs}}$, which means the rate of how many objective pions reached the most downstream counters of the spectrometer when we took account any disappearance caused by the reaction of the pions with the detector materials. We estimated $90.6 \pm 2.3\%$ for this rate, based on past experimental data near 995 MeV/c.

The effective solid angle, $\Delta\Omega_{\text{eff}}(\theta)$, which included the effects of pion decay and absorption, was written as follows:

$$\begin{aligned} \Delta\Omega_{\text{eff}}(\theta) &= \Delta\Omega(\theta)[1 - \varepsilon_{\text{de-es}}(\theta)](1 - \varepsilon_{\text{abs}}) \\ &= \Delta\Omega'_{\text{eff}}(\theta)(1 - \varepsilon_{\text{abs}}), \end{aligned} \quad (9)$$

where $\Delta\Omega(\theta)$ means the solid angle in the case of no decay and no absorption. Practically, we calculated the effective solid

TABLE II. Muon contamination ratio in the beam ($990 \text{ MeV}/c \leq P_\pi < 1000 \text{ MeV}/c$). The second column shows the experimental results by μ -GC at the target position and the statistical errors. The third column shows simulation results above threshold β by DECAY TURTLE [6] and the statistical errors. The fourth column shows the total simulation results involved above and below the threshold β . The first error is a statistical one, and the second is a systematic one. We assumed that the systematic error was the difference between the second column and the third column.

Setup for angular region	Experimental result by μ -GC (%)	Simulation result by DECAY TURTLE	
		Above threshold β (%)	Total (%)
π^- Beam			
Setup 1	3.7 ± 0.1	2.4 ± 0.1	$3.0 \pm 0.1 \pm 1.3$
Setup 2	4.8 ± 0.1	2.6 ± 0.1	$3.3 \pm 0.1 \pm 2.2$
π^+ Beam			
Setup 1	4.5 ± 0.1	2.0 ± 0.1	$2.7 \pm 0.2 \pm 2.5$
Setup 2	4.3 ± 0.1	2.3 ± 0.1	$3.0 \pm 0.1 \pm 2.0$

angle while considering the effect of the generated and escaped muons from the effective detector volume, $\Delta\Omega'_{\text{eff}}(\theta)$, using the simulation code GEANT. The physical processes of the energy loss, multiple scattering, and pion decay to a muon were considered in the calculation. The hadronic process was not included in calculating of $\Delta\Omega'_{\text{eff}}(\theta)$, because we treated

the nonabsorption rate of scattered pions, $1 - \varepsilon_{\text{abs}}$, separately. The event generator reproduced the position, direction, and momentum of the beam profile in the target. Events were generated uniformly for $(d \cos \theta)$ from $\theta - \frac{1}{2}\Delta\theta$ to $\theta + \frac{1}{2}\Delta\theta$ of the polar angle and for $d\phi$ from 0 to 2π of the azimuthal angle.

$$\Delta\Omega'_{\text{eff}}(\theta) = \left(\int_{\theta - \frac{1}{2}\Delta\theta}^{\theta + \frac{1}{2}\Delta\theta} d \cos \theta \int_0^{2\pi} d\phi \right) \times \left(\frac{\text{number of events accepted in trigger through effective detector volume}}{\text{number of events generated}} \right). \quad (10)$$

In the numerator, the pion decayed event to a muon in the effective detector volume is involved, except for a muon that escaped from the effective detector volume.

IV. EXPERIMENTAL RESULTS AND THE UNCERTAINTIES

The center-of-mass (c.m.) differential cross sections obtained for $\pi^+{}^{-12}\text{C}$ and $\pi^-{}^{-12}\text{C}$ elastic and inelastic scattering to 2_1^+ (4.44 MeV) are listed in Tables III and IV. Figure 5

shows the angular distributions of $\pi^+{}^{-12}\text{C}$ and $\pi^-{}^{-12}\text{C}$ elastic scattering. Figure 6 shows the angular distributions of inelastic scattering to 2_1^+ (4.44 MeV). In these figures the error bars represent the quadratic sum of the statistical and systematic errors.

The angular distribution was deduced for each 1° bin in the laboratory angle. The absolute angle has a systematic error derived from the setting angle of the SKS superconducting magnet. From empty run analysis, the ambiguity was estimated to be 0.2° . The statistical error includes all but two of the

TABLE III. Differential cross section for $\pi^+{}^{-12}\text{C}$.

c.m. angle and error $\theta_{\text{c.m.}} - \text{center}$ (deg)	Elastic c.m. cross section				2_1^+ (4.44 MeV) c.m. cross section			
	$\frac{d\sigma}{d\Omega}$ (mb/sr)	Stat. error ^a	Sys. error ^b	Total error	$\frac{d\sigma}{d\Omega}$ (mb/sr)	Stat. error ^a	Sys. error ^b	Total error
5.4±0.2	929	119	192	225				
6.5±0.2	775	42	93	102				
7.6±0.2	625	24	47	53				
8.7±0.2	444	15	25	29				
9.8±0.2	290	9.6	15	18				
10.9±0.2	184	6.7	9.2	11				
11.9±0.2	117	4.9	6.3	8.0				
13.0±0.2	76.5	2.1	7.0	7.3				
14.1±0.2	44.0	0.93	3.0	3.2				
15.2±0.2	20.4	0.42	1.4	1.5	13.1	0.32	1.3	1.3
16.3±0.2	8.50	0.21	0.64	0.68	11.3	0.27	1.1	1.2
17.4±0.2	2.60	0.11	0.21	0.24	9.08	0.23	0.98	1.0
18.4±0.2	0.616	0.052	0.098	0.11	6.36	0.18	0.70	0.72
19.5±0.2	0.352	0.040	0.058	0.071	4.58	0.15	0.51	0.53
20.6±0.2	0.752	0.059	0.071	0.092	3.04	0.12	0.36	0.38
21.7±0.2	1.32	0.078	0.076	0.11	1.78	0.096	0.18	0.21
22.8±0.2	1.61	0.087	0.12	0.15	1.09	0.080	0.12	0.14
23.8±0.2	1.76	0.090	0.16	0.18				
24.9±0.2	1.60	0.090	0.14	0.16				
26.0±0.2	1.19	0.075	0.094	0.12				
27.1±0.2	0.820	0.063	0.067	0.092				
28.2±0.2	0.571	0.057	0.060	0.082				

^aStatistical error.

^bSystematic error.

TABLE IV. Differential cross section for π^- - ^{12}C .

c.m. angle and error $\theta_{\text{c.m.}-\text{center}}$ (deg)	Elastic c.m. cross section				2_1^+ (4.44 MeV) c.m. cross section			
	$\frac{d\sigma}{d\Omega}$ (mb/sr)	Stat. error ^a	Sys. error ^b	Total error	$\frac{d\sigma}{d\Omega}$ (mb/sr)	Stat. error ^a	Sys. error ^b	Total error
5.4±0.2	985	134	141	194				
6.5±0.2	784	60	79	99				
7.6±0.2	630	36	47	59				
8.7±0.2	415	20	23	31				
9.8±0.2	298	14	15	21				
10.9±0.2	195	9.8	9.1	13				
11.9±0.2	123	2.9	11	11				
13.0±0.2	74.6	1.5	4.8	5.1				
14.1±0.2	41.4	0.82	2.8	3.0				
15.2±0.2	19.4	0.45	1.5	1.5	12.6	0.36	1.2	1.3
16.3±0.2	7.89	0.24	0.54	0.59	10.6	0.31	1.1	1.2
17.4±0.2	2.18	0.12	0.28	0.30	8.97	0.28	0.98	1.0
18.4±0.2	0.558	0.069	0.12	0.14	6.00	0.22	0.71	0.74
19.5±0.2	0.167	0.042	0.097	0.11	4.30	0.18	0.50	0.53
20.6±0.2	0.693	0.074	0.058	0.094	3.05	0.15	0.35	0.38
21.7±0.2	1.36	0.10	0.087	0.13	1.78	0.12	0.21	0.24
22.8±0.2	1.61	0.11	0.11	0.15	0.853	0.098	0.092	0.13
23.8±0.2	1.59	0.11	0.14	0.18				
24.9±0.2	1.32	0.098	0.11	0.15				
26.0±0.2	0.882	0.077	0.073	0.11				
27.1±0.2	0.730	0.075	0.12	0.14				
28.2±0.2	0.450	0.057	0.036	0.068				

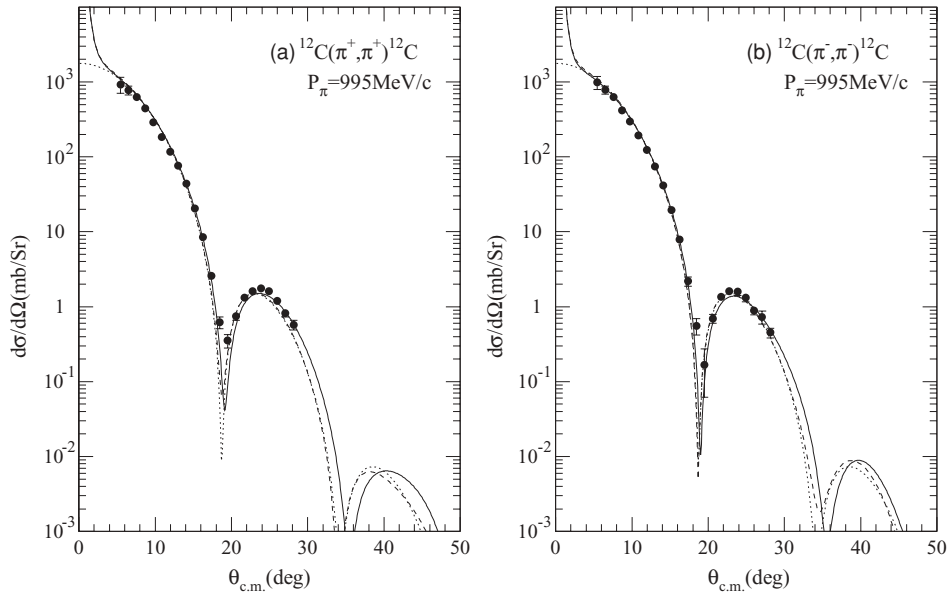
^aStatistical error.^bSystematic error.

FIG. 5. Differential cross section for elastic scattering, (a) $^{12}\text{C}(\pi^+, \pi^+)^{12}\text{C}$ and (b) $^{12}\text{C}(\pi^-, \pi^-)^{12}\text{C}$. The dashed curves show the results of PIPIT calculations with free elementary amplitudes, taking into account the Coulomb interaction. The solid curves represent the calculations with the fitted π - N elementary amplitudes, taking into account the Coulomb interaction. The dotted curves show the results of PIPIT calculations with free elementary amplitudes and ignoring the Coulomb interaction.

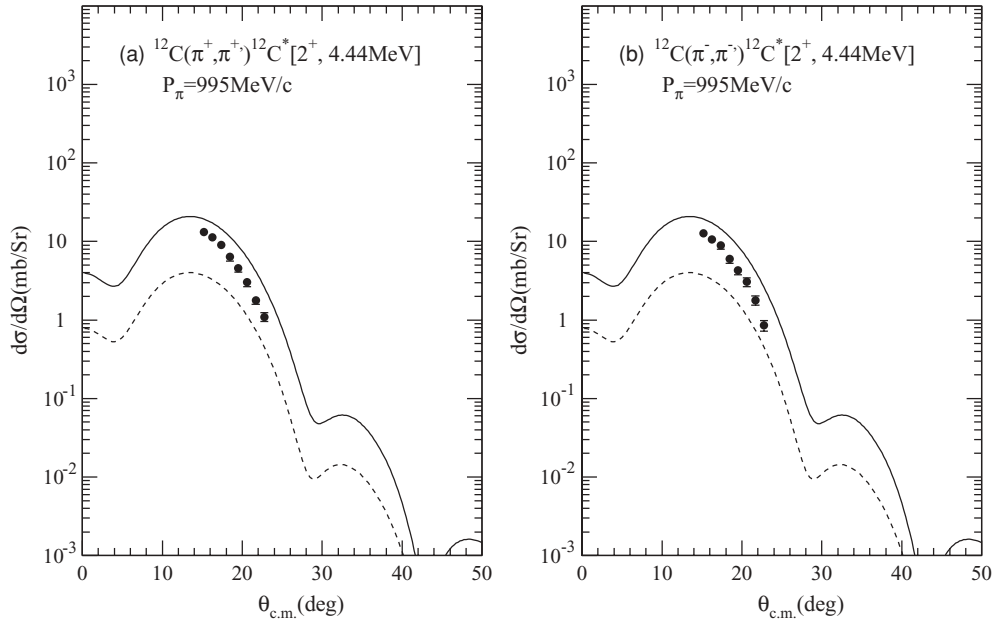


FIG. 6. Differential cross section for inelastic scattering (a) $^{12}\text{C}(\pi^+, \pi^+)^{12}\text{C}^*[2^+, 4.44 \text{ MeV}]$ and (b) $^{12}\text{C}(\pi^-, \pi^-)^{12}\text{C}^*[2^+, 4.44 \text{ MeV}]$. The solid lines represent the DWIA calculation results excluding the spin-flip effect, which was calculated by the transition density of the cluster-model wave function introduced by Kamimura. The dashed lines indicate the DWIA calculation results including the spin-flip effect without an effective charge, which were calculated by the Cohen-Kurath shell-model wave function. The Coulomb interaction was not included in either calculation.

efficiency errors. In Table I, the efficiency errors, except for the pion-muon ratio in beam ($R_{\pi\mu}$) and nonabsorption rate of scattering pion ($1-\varepsilon_{\text{abs}}$), were calculated statistically.

The systematic error includes the following errors:

- (i) There were some uncertainties derived from a discrepancy of 0.05° between the angular setup 1 and 2 setting angle analysis of the SKS. These were considered for the systematic error in a cross section analysis. The typical value of these uncertainties was 4.6% at $\theta_{\text{lab.}} = 14^\circ$ of $\pi^-^{12}\text{C}$.
- (ii) The systematic error of the pion-muon ratio in the beam ($R_{\pi\mu}$) was 2.2% at $\pi^-^{12}\text{C}$ angular setup 2, which is given in Table I.
- (iii) The systematic error of the nonabsorption rate of scattering pion ($1-\varepsilon_{\text{abs}}$) was 2.3% at $\pi^-^{12}\text{C}$ angular setup 2, which is given in Table I.
- (iv) For the elastic cross section of $\pi^+^{12}\text{C}$ and $\pi^-^{12}\text{C}$ in Tables III and IV, the fitting function error was included in the systematic error (5.1% at $\pi^-^{12}\text{C}$ angular setup 2) as an uncertainty. For the cross section of 2_1^+ (4.44 MeV), the uncertainty derived from fitting functions was also included in the systematic error (less than 6.3%), which was affected by the tail of the dominant ground state.

Table V and Fig. 7 show the π^+-p and $\pi^- -p$ center-of-mass differential cross sections that we measured using a scintillator target. The solid lines in Fig. 7 show the results of a phase-shift analysis calculation of the SAID [8] current solution. The dashed lines represent calculations of the SAID

KH80 solution. KH80 is an updated version of Höhler's phase shift (KH78 partial wave amplitudes) [9]. In this incident momentum region (995 MeV/c), the KH80 amplitudes are identical with the KH78 amplitudes. The agreement of our data with the calculations provides confirmation that our estimates of the absolute magnitude of the cross sections is correct (at least to $\sim 10\%$).

V. ANALYSIS AND DISCUSSION

In Fig. 5, we show the elastic cross section of $\pi^+^{12}\text{C}$ and $\pi^-^{12}\text{C}$. The dashed lines show the PIPIT calculations with free elementary amplitudes, taking account of the Coulomb interaction. PIPIT is a momentum-space optical potential code for pions based on a first-order optical potential model factorized as $t\rho$. In this calculation, we used:

- (i) Höhler's phase shift (KH78) up to the h -wave.
- (ii) The sum of the Gaussians (SOG) charge-density distribution parameters compiled by H. de Vries *et al.* [10] for ^{12}C . We obtained the point proton density by unfolding the charge density. We also assumed that the point neutron density is the same as the point proton density.
- (iii) A Gaussian-type off-shell extrapolation of the t -matrix.
- (iv) A nucleon form factor of $G(t) = [1.0 - t/0.71(\text{GeV}^2)]^{-2}$ [11] for unfolding the point proton densities from the charge-density distribution.

In both the elastic cross section of $\pi^+^{12}\text{C}$ and $\pi^-^{12}\text{C}$ at 995 MeV/c, PIPIT calculations well reproduce the magnitudes of the experimental cross sections.

TABLE V. Differential cross section for π^+p and π^-p .

c.m. angle and error $\theta_{\text{c.m.}-\text{center}}$ (deg)	π^+ c.m. cross section				π^- c.m. cross section			
	$\frac{d\sigma}{d\Omega}$ (mb/sr)	Stat. error ^a	Sys. error ^b	Total error	$\frac{d\sigma}{d\Omega}$ (mb/sr)	Stat. error ^a	Sys. error ^b	Total error
12.4±0.3	4.17	0.86	0.33	0.92	17.0	2.62	1.71	3.13
14.2±0.3	3.74	0.57	0.46	0.73	15.0	1.57	1.23	2.00
15.9±0.3	3.21	0.48	0.24	0.54	14.0	1.27	1.01	1.62
17.7±0.3	3.16	0.40	0.30	0.50	13.8	1.12	0.81	1.38
19.4±0.3	3.16	0.40	0.23	0.46	12.5	1.02	0.65	1.21
21.2±0.3	3.08	0.34	0.23	0.41	11.4	0.68	0.55	0.87
22.9±0.3	2.54	0.34	0.15	0.37	10.1	0.56	0.44	0.71
24.6±0.3	3.09	0.32	0.19	0.37	9.90	0.56	0.46	0.73
26.4±0.3	2.76	0.28	0.18	0.33	8.51	0.53	0.34	0.63
28.1±0.3	2.87	0.26	0.18	0.32	8.50	0.55	0.39	0.67
29.8±0.3	2.69	0.26	0.17	0.31	6.81	0.48	0.31	0.57
31.5±0.3	2.41	0.25	0.21	0.33	5.85	0.46	0.34	0.57
33.2±0.3	2.24	0.25	0.14	0.29	5.04	0.44	0.43	0.62
34.8±0.3	2.20	0.24	0.17	0.29	5.16	0.45	0.23	0.51
36.5±0.3	2.06	0.24	0.20	0.31	4.46	0.43	0.17	0.46
38.2±0.3	2.81	0.27	0.17	0.32	4.42	0.44	0.32	0.54
39.8±0.3	2.56	0.27	0.19	0.33	3.35	0.38	0.16	0.41
41.5±0.3	2.38	0.27	0.17	0.32	3.67	0.42	0.28	0.50
43.1±0.3	1.97	0.25	0.13	0.28	2.48	0.35	0.34	0.48
44.7±0.3	1.96	0.24	0.12	0.27	1.86	0.31	0.20	0.37
46.3±0.3	1.90	0.26	0.14	0.29				
47.9±0.3	1.30	0.22	0.067	0.23				
49.5±0.3	1.47	0.25	0.15	0.29				
51.0±0.3	1.58	0.32	0.20	0.38				

^aStatistical error.^bSystematic error.

In Fig. 5, the dotted curves represent the PIPIT calculations with free elementary amplitudes, ignoring the Coulomb interaction. Compared with the experimental data, it seems that there is almost no difference in the experimental data region between both PIPIT calculations with and without the Coulomb interaction.

To obtain the total cross section, the elastic cross section and the reaction cross section, we modified the elementary amplitudes. As is Ref. [3], we fitted the angular distributions by modifying the π - N elementary amplitudes with two

parameters, a_R and a_I , as follows:

$$\text{Re} \tilde{f}_{Ij}^l = a_R \text{Re} f_{Ij}^l, \quad \text{Im} \tilde{f}_{Ij}^l = a_I \text{Im} f_{Ij}^l, \quad (11)$$

where f_{Ij}^l is the free elementary amplitudes, and superscript l and subscripts Ij represent the orbital angular momentum, isospin, and total angular momentum in the total π - N system, respectively [12]. The optimum values of a_R and a_I were searched using the MINUIT program [13]. In a least-squares fit, the total χ^2 is defined as total $\chi^2(\alpha) =$

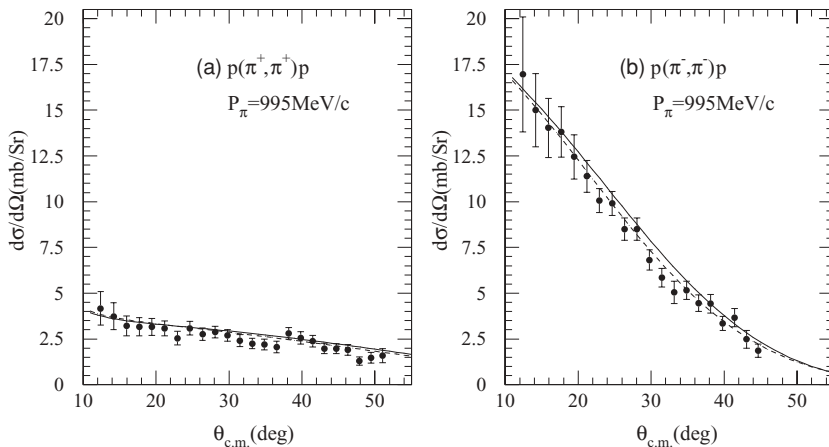


FIG. 7. Differential cross section for (a) $p(\pi^+, \pi^+)p$ and (b) $p(\pi^-, \pi^-)p$ measured with the scintillator target. The solid lines show the results of SAID calculations with the current solution and the dashed lines show the results of SAID calculations with KH80 solution that has the same amplitudes with Höhler's phase shift (KH78 partial wave amplitudes) in this incident momentum region (995 MeV/c).

TABLE VI. Ratio of the fitted amplitudes to the free one and the extracted cross sections.

Scattering	a_R	a_I	σ_{tot} (mb)	σ_{el} (mb)	σ_R (mb)
$^{12}\text{C}(\pi^+, \pi^+)^{12}\text{C}$	+0.27	+0.04	+9.3	+4.1	+5.2
	-0.33	-0.04	-10.1	-4.4	-5.7
$^{12}\text{C}(\pi^-, \pi^-)^{12}\text{C}$	+0.20	+0.03	+6.3	+2.9	+3.5
	-0.23	-0.03	-6.6	-3.0	-3.7

$\sum_{i=1}^n (f(x_i, \alpha) - e_i)^2 / s_i^2$, where α is the vector of the free parameters being searched and s_i are the uncertainties in the individual measurements, e_i . We used the square root of a quadratic sum of the statistical and systematic errors of the measured differential cross section for s_i . The total cross section (σ_{tot}), elastic cross section (σ_{el}), and reaction cross section (σ_R) were extracted from the nuclear part of the scattering amplitude in this model, separating the Coulomb potential part from the total scattering amplitude. The errors of the σ_{tot} , σ_{el} , and σ_R were defined in our model as follows:

(i) In the case of the two-parameter fitting for reduced $\chi^2 = 1$, the one standard deviation region ($\approx 68.3\%$) is defined by

$$\text{total } \chi^2 < (N - F) + \text{UP}, \quad (12)$$

where

$$\begin{aligned} N &= \text{number of the data,} \\ F &= \text{number of the parameter,} \end{aligned}$$

and $\text{UP} = 2.30$ [14].

(ii) In our cases, the reduced χ^2 is larger than 1, and typical values are 3.4 for $\pi^+ - ^{12}\text{C}$ and 1.5 for $\pi^- - ^{12}\text{C}$. The reason that reduced $\chi^2 > 1$ is attributed to an inadequacy of the model. If the model were suitable, it would realize reduced $\chi^2 = 1$. To compensate for the inadequacy, we decided to increase the errors artificially to realize reduced $\chi^2 = 1$. In practice, we adopted the artificially increased UP' to evaluate the error from

the inadequacy of the model. This means that we redefined the region of the standard deviation by the following equation:

$$\text{total } \chi^2 < \text{minimum of the total } \chi^2 + \text{UP}', \quad (13)$$

where

$$\begin{aligned} \text{minimum of the total } \chi^2 &= \text{reduced } \chi^2 \times (N - F) \\ \text{UP}' &= \text{reduced } \chi^2 \times \text{UP}, \text{UP} = 2.30. \end{aligned}$$

(iii) In such a two-parameter problem of our model, we defined the errors for σ_{tot} , σ_{el} , and σ_R as the minimum and the maximum values that are allowed by the above total χ^2 condition.

The best-fit values are listed in Table VI. The solid lines in Fig. 5 show the fitted results with modified π - N elementary amplitudes. In Fig. 8, these extracted cross sections are plotted together with previously reported data [2,3,15–18]. The dashed lines in the figures show the results of PIPIT calculations with free elementary amplitudes. It seems that our results (solid triangle) show a slightly smeared resonance. In the forward angle of Fig. 5, the PIPIT calculations with modified π - N elementary amplitudes agree well with that by free elementary amplitudes. Because we used the optical theorem to deduce the total cross section, it is natural that our extracted cross sections are close to the PIPIT calculation with the free elementary amplitudes.

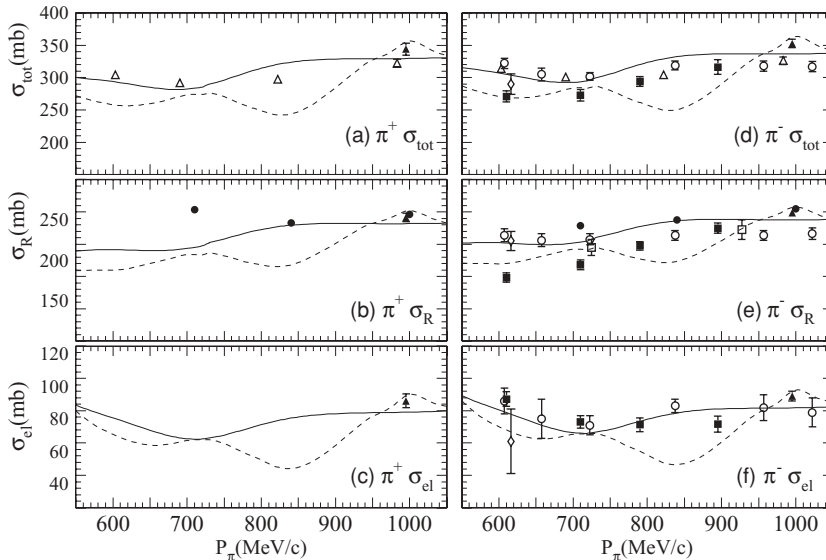


FIG. 8. Incident momentum dependence of (a) σ_{tot} , (b) σ_R , and (c) σ_{el} for $^{12}\text{C}(\pi^+, \pi^+)^{12}\text{C}$ and (d) σ_{tot} , (e) σ_R , and (f) σ_{el} for $^{12}\text{C}(\pi^-, \pi^-)^{12}\text{C}$. Our data (solid triangle) are plotted with the data of Clough *et al.* [15] (open triangle), Allardyce *et al.* [16] (solid circle), Takahashi *et al.* [3] (solid square), Crozon *et al.* [17] (open circle), Cronin *et al.* [18] (open square), and Gelderloos *et al.* [2] (open diamond). The dashed lines show the results of PIPIT calculations with free elementary amplitudes. The solid lines represent the results of taking into account the effect of Fermi motion.

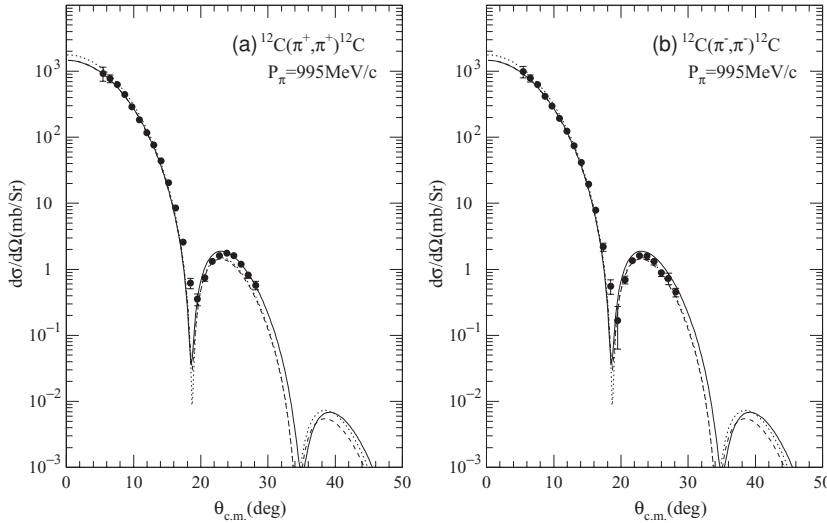


FIG. 9. Differential cross section for elastic scattering with three theoretical calculations: (a) $^{12}\text{C}(\pi^+, \pi^+)^{12}\text{C}$ and (b) $^{12}\text{C}(\pi^-, \pi^-)^{12}\text{C}$. The dot curves show the results of PIPIT calculations with free elementary amplitudes. The solid curves represent the cluster-model calculations introduced by Kamimura. The dashed curves represent the extreme single-particle shell-model calculations. The Coulomb interaction was not considered for all calculations.

To explain the smeared resonance, we estimated the effect of Fermi motion by averaging the elementary amplitude in the center-of-mass frame (f_{lj}^l) for each partial wave, denoted by (l, l, j) . To obtain the averaged elementary amplitude in the center-of-mass frame (\tilde{f}_{lj}^l), we transformed the nucleon momentum (k) and the Fermi momentum (k_F) into the center-of-mass frame and calculated:

$$\tilde{f}_{lj}^l[s(0)] = \frac{\int_{k_{c.m.} \leq k_{F.c.m.}} f_{lj}^l d\mathbf{k}_{c.m.}}{\int_{k_{c.m.} \leq k_{F.c.m.}} d\mathbf{k}_{c.m.}}, \quad (14)$$

$$s(\mathbf{p}_N) = m_\pi^2 + m_N^2 + 2(E_\pi E_N - \mathbf{p}_\pi \cdot \mathbf{p}_N), \quad (15)$$

where $k_{c.m.}$ and $k_{F.c.m.}$ represent the transformed nucleon momentum and the Fermi momentum in the center-of-mass frame. In this calculation, we took k_F as 270 MeV/ c (nuclear matter) in the laboratory frame. In Fig. 8, the solid lines show the PIPIT calculation results using these Fermi-averaged amplitudes. It seems that the effect of Fermi motion explains the overall tendency.

Figure 9 shows a comparison of the elastic cross-section data of $\pi^+ - ^{12}\text{C}$ and $\pi^- - ^{12}\text{C}$ with three theoretical calculations. The dot curves show the results of PIPIT calculations with free elementary amplitudes. The solid curves and dashed curves represent the momentum-space optical calculations using the cluster-model density derived by Kamimura [19] and using the extreme single-particle model density of ^{12}C , respectively. The Coulomb interaction was not considered for these three calculations. All three calculations are in nearly good agreement with our data.

Figure 6 shows the $2_1^+(4.44 \text{ MeV})$ inelastic cross-section data of $\pi^+ - ^{12}\text{C}$ and $\pi^- - ^{12}\text{C}$ and the DWIA calculations. Because the DWIA calculations ignore the Coulomb interaction, π^+ and π^- calculations show the same value. We confirmed that there was no visible difference in the PIPIT elastic calculations for the experimental data region of Fig. 5 between the calculations with and without the Coulomb interaction. For this reaction in the angular range investigated, the spin-flip contribution is very small, making no visible difference there for the Cohen-Kurath calculation in Fig. 6. The solid lines indicate the DWIA calculation results, excluding the spin-flip

effect, which were calculated with the transition density of the cluster-model wave function introduced by Kamimura. Its transition density is expressed by a Gaussian-type expansion of 12 terms [19]. Kamimura's cluster-model wave function reproduces the transition form factor of electron scattering and is thought to be the most elaborate nuclear wave function for ^{12}C . The discrepancy may be attributed to the treatment of the nuclear reaction process [20]. The dashed lines in Fig. 6 indicate the calculation results, including the spin-flip effect without any effective charge, which were calculated by the Cohen-Kurath shell-model wave function [21]. If we use 1.85 for the effective charge for the shell-model calculations, the calculation results can reproduce our experimental data. This value of 1.85 for the effective charge is larger than the commonly accepted values, $\sqrt{2}$ [22,23]. This means that the commonly accepted effective charge cannot explain our experimental data.

Except for the absolute value, both DWIA calculations reproduced the feature of the experimental data. As for the absolute value, the cluster-model calculation is about two times larger than the experimental data. However, the shell-model calculation result is less than the experimental data.

Both of the DWIA calculations used the momentum-space optical potential method [24,25] without considering the couplings of the pion partial waves by quadrupole deformation of $^{12}\text{C}(2_1^+)$.

Thus, both of the theoretical calculations cannot reproduce the absolute value for the 2_1^+ (4.44 MeV) inelastic cross section of $\pi^+ - ^{12}\text{C}$ and $\pi^- - ^{12}\text{C}$. This means that further theoretical study, including the reaction process, is necessary for the excited states of the ^{12}C nucleus.

VI. SUMMARY

We measured the angular distributions of the differential cross sections for $\pi^+ - ^{12}\text{C}$ and $\pi^- - ^{12}\text{C}$ elastic scattering and inelastic scattering to the 2_1^+ (4.44 MeV) state at an incident pion momentum of 995 MeV/ c using the SKS. We paid special attention to deduce precise values for the absolute cross sections. The systematic errors of the absolute cross

sections for both elastic and inelastic scattering are small. The magnitude of the absolute cross sections were confirmed by comparing the $\pi^+ - p$ and $\pi^- - p$ differential cross sections under the same trigger and data reduction conditions. These data agree well with the phase-shift analysis calculations (SAID).

Our data for elastic scattering of $\pi^+ - {}^{12}\text{C}$ and $\pi^- - {}^{12}\text{C}$ were, overall, reproduced by a first-order factorized momentum-space optical potential calculation with free $\pi - N$ elementary amplitudes (PIPIT). By modifying the elementary amplitudes, we further extracted σ_{tot} , σ_{el} , and σ_R phenomenologically. These cross sections are lower than those obtained by PIPIT calculations using the free elementary amplitude. We estimated the effect of Fermi motion by averaging the $\pi - N$ elementary amplitude to explain them.

We also compared our elastic data with the momentum-space optical potential calculation using different nuclear densities. One was a nuclear density deduced from the cluster model derived by Kamimura, and the other was deduced from the extreme single-particle shell model. These two calculations reproduced well our elastic data too.

For the 2_1^+ (4.44 MeV) inelastic cross section of $\pi^+ - {}^{12}\text{C}$ and $\pi^- - {}^{12}\text{C}$, we compared our data with two DWIA calculations. One used the cluster model transition density introduced by Kamimura, and the other used the transition density by the

Cohen-Kurath shell model. In spite of the good agreements of the elastic data, these two calculations did not reproduce the absolute magnitude of our inelastic data. The cluster-model calculations overestimated the experimental value. However, the shell-model calculations underestimated the experimental value. Further theoretical investigations including the reaction process are necessary to explain the cross sections for the excited states of the ${}^{12}\text{C}$ nucleus.

ACKNOWLEDGMENTS

The authors express great appreciation to the staff of the KEK 12 GeV-PS for their support in running this experiment. We are grateful to Professor K. Nakai, who encouraged us during this experiment. We also thank Professor M. Ieiri who advised us concerning the beam transportation. We are deeply obliged to Professor T. Shintomi, Professor Y. Doi, Professor Y. Makida, Mr. Y. Kondo, and other cryogenic group members for their contributions and efforts to construct and maintain the SKS superconducting magnet and the cryogenic system, which are the key techniques of this experiment. We are indebted to Professor M. Arima for an offer of the calculation code as well as discussions. We also express our gratitude to Professor M. Kamimura for helpful advice about theoretical matters.

-
- [1] D. Marlow *et al.*, Phys. Rev. C **30**, 1662 (1984).
 - [2] C. J. Gelderloos *et al.*, Phys. Rev. C **62**, 024612 (2000).
 - [3] T. Takahashi, H. Sakaguchi, K. Aoki *et al.*, Phys. Rev. C **51**, 2542 (1995).
 - [4] R. A. Eisenstein and F. Tabakin, Comput. Phys. Commun. **12**, 237 (1976).
 - [5] T. Fukuda *et al.*, Nucl. Instrum. Methods A **361**, 485 (1995).
 - [6] K. L. Brown *et al.*, Report No. CERN 74-2, 1974.
 - [7] CERN Program Library Long Writeup W5013, GEANT.
 - [8] R. A. Arndt *et al.*, computer code SAID, <http://gwadac.phys.gwu.edu/>.
 - [9] G. Höhler, in *Pion Nucleon Scattering*, edited by H. Schopper, Landolt-Börnstein, New Series, Group I, Vol. 9b. Pt. 2 (Springer-Verlag, Berlin, 1983).
 - [10] H. de Vries, C. W. de Jager, and C. de Vries, At. Data Nucl. Data Tables **36**, 495 (1987).
 - [11] H. Pilkuhn, in *Particle Properties, Coupling Constants and Form Factors*, edited by H. Schopper, Landolt-Börnstein, New Series, Group I, Vol. 6. Pt. 1 (Springer-Verlag, Berlin, 1972).
 - [12] M. Arima, K. Masutani, and R. Seki, Phys. Rev. C **44**, 415 (1991).
 - [13] CERN Program Library Long Writeup D506, MINUIT.
 - [14] P. R. Bevington and D. K. Robinson, *Data Reduction and Error Analysis for the Physical Sciences*, 3rd ed. (McGraw-Hill, New York, 2003).
 - [15] A. S. Clough *et al.*, Nucl. Phys. **B76**, 15 (1974).
 - [16] B. W. Allardyce *et al.*, Nucl. Phys. **A209**, 1 (1973).
 - [17] M. Crozon, Ph. Chavanon, A. Courau, Th. Leray, J. L. Narjoux, and J. Tocqueville, Nucl. Phys. **64**, 567 (1965).
 - [18] J. W. Cronin, R. Cool, and A. Abashian, Phys. Rev. **107**, 1121 (1957).
 - [19] M. Kamimura, Nucl. Phys. **A351**, 456 (1980) and private communication.
 - [20] N. Nose, K. Kume, and S. Yamaguchi, Phys. Rev. C **50**, 321 (1994).
 - [21] S. Cohen and D. Kurath, Nucl. Phys. **73**, 1 (1965).
 - [22] J. B. Flanz, R. S. Hicks, R. A. Lindgren, G. A. Peterson, A. Hotta, B. Parker, and R. C. York, Phys. Rev. Lett. **41**, 1642 (1978).
 - [23] K. H. Hicks *et al.*, Phys. Rev. C **38**, 229 (1988).
 - [24] M. I. Haftel and F. Tabakin, Nucl. Phys. **A158**, 1 (1970).
 - [25] N. Nose-Togawa and K. Kume, Phys. Rev. C **59**, 2162 (1999).